

# Reconstruction of coseismic slip from the 2015 Illapel earthquake using combined geodetic and tsunami waveform data

Amy Williamson<sup>a,\*</sup>, Andrew Newman<sup>a</sup>, Phil Cummins<sup>b</sup>

<sup>a</sup> School of Earth and Atmospheric Sciences, Georgia Institute of Technology, 311 Ferst Drive, Atlanta, GA, 30332, United States

<sup>b</sup> Research School of Earth Sciences, Australian National University, Canberra, ACT, Australia

\* Corresponding author. E-mail address: [amy.williamson@gatech.edu](mailto:amy.williamson@gatech.edu) (A. Williamson)

## Key Points

- Combined tsunami and land-based geodetic inversions can offer improved seismogenic fault resolution for tsunamigenic megathrust earthquakes.
- 2015 Illapel earthquake excited substantial tsunami waves observed across Pacific-South America, with transoceanic records as far as Kuril Islands.
- Inverse model shows most slip in 2015 Illapel earthquake occurs just offshore, with little near-trench contribution required.

## Abstract

On 16 September 2015, a moment magnitude ( $M_w$ ) 8.3 earthquake struck off the coast of central Chile, generating a large tsunami with nearby coastal wave heights observed on tide gauges in Chile and Peru of up to 4.7 m, and distal observations of over 40 cm in the Kuril Islands across the Pacific Ocean. Through a trans-coastal geodetic study, including tsunami time series recorded at open-ocean pressure gauges, sub-aerial deformation observed through Interferometric Synthetic Aperture Radar (InSAR) from the Sentinel-1 A satellite and continuous GPS, we identify the location and extent of coseismic slip. We find that most coseismic slip was concentrated in a patch immediately offshore, with little modeled slip near the trench. This result satisfies the tsunami waveforms measured in the deep ocean north of the rupture area, with wave heights up to 10 cm. While the event exhibits some features of a slow tsunami earthquake (moderately large tsunami and possible slow second-stage rupture), our inversion results do not require substantial near-trench rupture. However, the prevalence of large and shallow thrust along subduction megathrusts along central Chile raises the question of the likelihood of future such events and the implications for future hazardous tsunamigenic earthquakes.

## Keywords

Chile, tsunami, Illapel, subduction zone, joint inversion

This article has been accepted for publication and undergone full peer review but has not been through the copyediting, typesetting, pagination and proofreading process which may lead to differences between this version and the Version of Record. Please cite this article as doi: 10.1002/2016JB013883

## 1. Introduction

Over the past century, the Peru-Chile trench has produced many great tsunamigenic earthquakes and has been the focus of several studies of subduction zone earthquake excitation, tectonic strain accumulation, and interseismic coupling [Vigny *et al.*, 2009; Moreno *et al.*, 2010; Moreno *et al.*, 2011]. This propensity for large events is in part fueled by the region's rapid plate motion. In the vicinity of central Chile, the Nazca plate subducts beneath the South American plate with a rate of convergence of 74 mm/yr [DeMets *et al.*, 2010]. Many of the more recent earthquakes in the region have produced tsunamis that have been recorded at coastal tide gauges as well as at deep ocean pressure sensors as shown in Figure 1.

One problem in determining the extent of slip from megathrust events is having a clearly resolved domain that extends past the coast to the trench. This shallow, submarine zone is oftentimes poorly resolved through purely geodetic datasets, where many different rupture models can provide equally satisfactory fits to observed data. However, the inclusion of tsunami data, particularly as recorded away from the source at deep ocean pressure gauges, adds a resolvability in this shallow zone that is sensitive to tsunami excitation.

The tsunami generated from a large earthquake is a function of the amount of slip occurring underwater, which for many cases translates to the amount of slip occurring within a shallow (< 30 km depth) part of the megathrust. Tsunami waveforms are therefore a good proxy for understanding this shallow, near trench environment, which for many regions lacks direct observation by instrumentation. This can be particularly important for a special subclass of earthquakes, aptly named tsunami earthquakes, which generate a much larger tsunami than expected from the derived magnitude, and are often deficient in radiating seismic energy while maintaining a characteristically slow rupture propagation [Kanamori, 1972]. The 1996 Chimbote, Peru earthquake, with a  $M_w$  of only 7.8, produced one meter-

level waves locally around Peru and Northern Chile, and waves up to 0.3 m near Easter Island, approximately 3800 km away, with up to a maximum run up height of almost 5 m. The disproportionately large tsunami generated by this event is partially a function of its rupture along the shallow part of the megathrust [Heinrich *et al.*, 1998]. Its source location and its deficiency in radiating high frequency energy led this event to be categorized as a tsunami earthquake by Newman and Okal [1998].

However, other tsunamigenic earthquakes in this region were recorded transoceanically without falling into the tsunami earthquake subclass. The largest-ever instrumentally recorded earthquake, occurring near Valdivia, Chile in 1960, generated a large and devastating transoceanic tsunami. Eyewitness observations near the source region suggest 10 to 15 m waves along the coast [NGDC, 2016]. On a regional scale, tide gauge recordings near the city of Concepción topped out with zero-to-crest amplitudes of over 2.5 m, and tide gauges in northern Chile and Peru (2,000 to 3,000 km away) recorded waves between 0.5 and 1 m in height [NGDC, 2016].

More recently, the 2010  $M_w$  8.8 Maule earthquake ruptured a patch of the megathrust just to the north of the 1960 Valdivia earthquake. In the near field, tide gauges recorded waves with amplitudes around 1 m, with the largest wave = 1.3 m occurring in a bay near the city of Coquimbo. Far field recordings in Peru were less than 0.5 m. Maximum on-land run-up heights reached 29 m at Tirua, 250 km from the source region. Nevertheless, the earthquake and tsunami created over 30 billion dollars in damage and resulted in over 500 casualties in Chile [USGS report; Fritz *et al.*, 2011]. Additionally, in 2014, the  $M_w$  8.1 Iquique earthquake in northern Chile, while smaller, also produced a regionally observable tsunami [An *et al.*, 2014; Gusman *et al.*, 2015].

The latest tsunamigenic addition to the Peru-Chile catalog is the 16 September 2015  $M_w$  8.3 Illapel earthquake. This event nucleated offshore from Coquimbo Province

(approximately  $31.57^{\circ}$  S and  $71.67^{\circ}$  W) at approximately 22:54:32 UTC. While the earthquake was smaller in size compared to other contemporary tsunamigenic earthquakes near Chile, including the 2010 Maule earthquake just to the south, it produced a locally large tsunami (up to 4.7 m near Coquimbo as measured by a local tide gauge). The tsunami was transoceanic, with tide gauges recordings throughout the Pacific basin, including Oahu, Hawaii (0.23 m), Kuril Islands, Russia (0.44 m), and Aburatsu, Japan (0.22 m).

The wide spectrum of tsunami generated by earthquakes on the Peru-Chile trench provides a rich and often under-utilized dataset for static source inversions. While previous studies of the Illapel earthquake have incorporated data from the tsunami, either from the nearby deep ocean pressure gauges, or the numerous tide gauges along the coast, this data has been used exclusively through forward models as a constraint on seismic or geodetic inversions or as a validation of a particular model [Calisto *et al.*, 2016; Heidarzadeh *et al.*, 2015; Li *et al.*, 2016; Tilmann *et al.*, 2016]. However, for many model results, the forward projection of the model results as a tsunami and its comparison to the observed data from deep ocean gauges is out of phase with observations by a few minutes and often miscalculates the peak amplitude of the first wave, as was shown well in Calisto *et al.* [2016]. While it is unlikely for any one model to well fit all datasets, this consistent phase delay should be addressed as it appears to transcend the type of tsunami propagation model used and the handling of the observed data.

To characterize the 2015 Illapel earthquake, we use Line-Of-Sight (LOS) Interferometric Synthetic Aperture Radar (InSAR) observations, static offsets from continuous GPS, and tsunami time series from the four nearest Deep Ocean Assessment and Reporting of Tsunamis (henceforth, DART) pressure gauges. As was originally shown in a combined tsunami-InSAR inversion by Gusman *et al.* [2010], we find that the combination of both land-based geodetic and tsunami datasets, which span the shoreline, allows for

maximum resolution of the earthquake slip environment across the subduction megathrust. As we detail below, through a joint inversion of both data types, we find that the maximum coseismic slip occurred in the down-dip near-coastal environment, providing the best fit in phase and amplitude to deep ocean time series and on-land static deformation. This moves the locus of dominant slip away from the near-trench environment. While this provides a better fit to the tsunami data, it is in contradiction to some past geodetic and seismic studies on the same event [Heidarzadeh *et al.*, 2015; Lee *et al.*, 2016; Li *et al.*, 2016; Ruiz *et al.*, 2016; Ye *et al.*, 2016].

## 2. Data

In this study we incorporate data from four nearby DART pressure gauges. Each gauge records the pressure of the overlying water column and translates this to water column height using a conversion constant at 15 minute, one minute, or 15 second sampling frequencies depending on if each gauge is in standby or a triggered event mode. With a sensitivity of less than one millimeter in deep-water, DART pressure gauges are ideal for measuring long period, low amplitude tsunami waves. Unlike coastal tide gauges which record the tsunami as it interacts with the coastline, leading to non-linear effects such as harbor resonance, DART gauges, because they are located in the deep-ocean, are largely immune to small scale bathymetric changes. We removed tides recorded at each station through polynomial fitting, then filtered the signals to remove high frequency surface wave energy. Additionally, we windowed each time series to only include the tsunami's arrival and first wavelength in the signal used for the inversion. This is of particular importance for the two nearest stations, where waves reflected from the coast appear early on in the time series.

We also use the LOS displacement field derived from a pair of descending track scenes (24 August and 17 September 2015) recorded by the Sentinel-1A SAR satellite, and

processed by the European Space Agency [*Copernicus Service information*, 2015]. The resultant InSAR image shows a maximum of 150 cm of ground deformation in the LOS direction. While we correct for changes in LOS look angle, we also tested a constant angle of  $41^\circ$  off nadir, near the maximum deformation and found the difference to be negligible.

Because the data density and interdependence of pixels is extremely high (on the order of  $10^7$  pixels per image), it was necessary for us to down-sample the field of data to make the image manageable for computational inversions. To do so, we use a two-dimensional Quadtree decomposition similar to *Jónsson et al.* [2002], that retains more information in environments that have more significant change. We require that each geographically oriented quadrangle containing InSAR signals is split into four smaller quadrangles whenever the variance in LOS displacement is greater than a set tolerance level (5% difference). For the remaining 1,200 boxes, we assign the average displacement to the ‘center of mass’ position of coherent pixels. The resulting down-sampled image, overlaying the original displacement field, is shown in Figure 2. Because the second pass follows one day after the event, any post-seismic signal is likely to remain small. Furthermore, because most observations of early afterslip occur primarily up-dip of the main rupture along subduction zones [e.g. *Hsu et al.*, 2006; *Malservisi et al.*, 2015], we suspect the land-based data to be more representative of co-seismic rupture.

Additionally, we incorporate static offsets from sixteen three-component continuous GPS stations, located in central Chile, operated by the National Seismological Center of the Universidad de Chile, with static displacements reported in *Ruiz et al.* [2016]. The dataset shows a consistent seaward motion by all stations and a small, but complex and comparably small vertical signal of uplift and subsidence at the coastal stations.

When constrained to the use of only land-based geodetic instruments such as GPS and InSAR, the shallow subduction zone region is generally too far offshore to be resolvable in

distributed-slip (i.e., “finite fault”) inversions. While seafloor geodetic instruments are feasible, they are often cost prohibitive and thus few regions currently have the infrastructure in place, causing many communities to forgo their use [Newman, 2011]. This leads to difficulty in constraining slip in this highly hazardous, but in these cases poorly resolved, zone. By supplementing this dataset with ocean-based observations, like tide gauge or pressure gauge time series, we find that spatial resolvability of the offshore region increases substantially (see Model Resolution, below).

### **3. Methods**

#### **3.1 Model Geometry**

We describe the source region with a three-dimensional curvi-planar fault geometry. We then discretize the modeled fault plane into a 575 x 200 km surface, consisting of a 23x8 grid, with individual patches of dimensions 25 km along strike and 25 km along dip. The strike and dip of the fault interface vary for each patch, approximating the profile created from Slab 1.0 [Hayes *et al.*, 2012]. While the inclusion of a strike variability does cause a small amount of overlap of patches, the total overlap is negligible in calculating the seismic moment.

#### **3.2 Inversion Technique**

We calculate Green’s functions for InSAR LOS displacements and GPS static offsets through an analytic solution to the elastodynamic equations for rectangular dislocations in an elastic half space [Okada, 1985]. For DART data, we generate Green’s functions relating fault slip by combining the vertical surface deformation from Okada [1985] with the tsunami propagation model, JAGURS [Baba *et al.*, 2015; Allgeyer and Cummins 2014]. JAGURS is a finite difference method model that, in addition to solving the non-linear shallow water wave

equations, has the ability to incorporate elastic loading, seawater compressibility, gravitational potential change and Boussinesq dispersion into the propagation simulation. In order to account for hydrodynamic effects that alter the pattern of displacement transmitted from the seafloor to sea surface, we applied a smoothing filter [Kajiura, 1963] was applied to the seafloor displacement of each subfault before it was translated to the sea surface. Finally, we perform a linear inversion for positive dip-slip motion (thrust) along our fault geometry, bounding to be less than 20 meters per fault patch. While the tsunami propagation code is non-linear, it is well behaved for open-ocean tsunami propagation, particularly in the near-field, making it amenable for inclusion in a bound linear inversion.

We relate our geodetic and tsunami Green's functions to fault interface slip through the model GTdef developed by *Chen et al.* [2009] and following *Jónsson et al.* [2002]. The model solves the linear system of equations using

$$\begin{bmatrix} w & d \\ 0 & \end{bmatrix} = \begin{bmatrix} w & G \\ \kappa^2 & D \end{bmatrix} m$$

where  $d$  is the observed data vector,  $G$  is the Green's function matrix,  $m$  is the vector of unknown slip on the fault,  $D$  is a finite difference smoothing operator that relates each patch with a weight regulated by  $\kappa$ . The Green's function matrix is composed of tsunami waveforms and static offsets from both LOS InSAR measurements as well as horizontal and vertical GPS measurements. Both the observation vector and the Green's function matrix are modified with a coefficient,  $w$ , representing measurement errors associated with each type of observation and a weight relating the different datasets. The total contribution of each dataset varies, with the number of discretized tsunami waveform data (10,800 points) exceeding Quadtree down-sampled InSAR data (1,200 points) and GPS data (16 sites x 3 components). To ensure comparable sensitivity between the tsunami and land-based geodetic data, we weighted the cumulative datasets equally for the inversion.

We regularize our solution using  $\kappa$  to force an interdependence between adjacent slip patches [Harris and Segall, 1987]. An increasing smoothing factor, acts as a trade-off with the misfit of the model. The misfit is determined as the root-mean square (RMS) of the weighted-residual sum of squares (WRSS). While an unconstrained model where each patch acts independently of its surrounds would theoretically provide the best fit to the observed data, solutions would be non-unique and would potentially provide unrealistically rough results. Instead, we evaluate a range of unique models constrained by increasing  $\kappa$  (Figure S1), before choosing our preferred model, determined by evaluating the trade-off between model misfit and roughness.

### 3.3 Model Resolution

We approximate the spatial resolvability of our model using a “checkerboard test,” consisting of 50 km by 50 km blocks with alternating predefined uniform slip magnitudes between 0 and 1 meter (Figure 3). Using these patches as input, we predict deformation at each data point for InSAR, GPS, and tsunami datasets as well as the combination of all three. We subsequently invert these synthetic data with our observed data error, and compare our inverted with our initial models. In areas where the checkerboard is retained, we have high resolvability.

The spatial resolution of the study region is assumed to vary due to a non-uniform distribution of observations. For geodetic (InSAR and GPS) checkerboard results, the best resolution is centered at  $71.5^\circ$  W and  $31^\circ$  S, about where the largest change in deformation both in InSAR and GPS offsets occurs. However, resolution is limited offshore and does not extend along strike through the study area. The tsunami dataset checkerboard result shows an excellent recreation of the checkerboard pattern offshore, but resolution is quickly lost for fault patches located under land, where slip would minimally affect the water column. The

checkerboard for the combined dataset has good resolution for almost the entire study region, excluding a patch down-dip and to the north of the main region of deformation, where there are few GPS stations and a small amount of change in the InSAR image, thus a smaller dataset. However, for the combination image, the checkerboard pattern was recovered for the region where we expect to see most slip from this earthquake.

#### **4. Results**

The majority of slip occurred in one main patch immediately offshore but not reaching the trench axis. The peak slip in our preferred model reaches 11 meters, while the main patch of consistent slip extends about 125 km along strike and 50 km along dip. This peak slip measurement is an estimate of the slip in the smoothed model, the value has the potential to change with a different smoothing factor. Forward projections of the GPS displacement vectors, InSAR LOS displacement fields, and tsunami waveforms are shown in Figures 4-6.

Our model is in good agreement with tsunami time series recorded at four nearby DART gauges (Figure 5), with little phase delay between the modeled tsunami arrival and the observed time series, and a consistent peak amplitude for the initial part of the tsunami, before the inclusions of coastal reflections. The fit of the model at the nearest gauge, DART 32402, also partially recreates the wave trough that was recorded about 50 minutes after the earthquake. This feature was not modeled in studies assessed in *Calisto et al.* [2016], *Heidarzadeh et al.* [2016], or *Tang et al.* [2016]. While the later, trailing part of the tsunami is not consistently recreated across all DART gauges, this part of the time series includes modulations of the tsunami from coastal reflections and inundation, which we do not confidently recreate in our tsunami Green's functions or forward tsunami model.

Forward projections of the geodetic data, both for the GPS stations and a recreation of the InSAR deformation both yield good results. The largest misfit within the geodetic datasets occurs close to the coastline where the preferred model slightly under predicts deformation.

## 5. Discussion

The addition of a tsunami dataset to the earthquake source inversion adds a spatial resolution to the solution, especially in the near-trench region. This is noticeable when comparing the arrival times of a tsunami at deep water gauges between models and observations. The inclusion of tsunami datasets also assists in constraining shallow slip, which may not be resolved well with land based datasets, and may also constrain seafloor uplift in a complex and often poorly understood part of the subduction zone.

This region has poor azimuthal coverage of DART gauges, they are only located to the north of the rupture area and oblique to the directivity of the tsunami. While a new station was added directly south of the Illapel earthquake during the fall of 2015, which could potentially aid in constraining the location of slip with further confidence, it was not fully deployed until after the event. Located near the trench axis, the close proximity of the gauge to the megathrust reduced the delay between the earthquake and the arrival of the tsunami at the station, increasing the time available to assess the tsunami for far-field hazard warnings. It also provides an opportunity for real-time or near-real-time source inversions incorporating tsunami data, and possibly supplementing other real-time source characterization methods [Benavente *et al.*, 2016].

Ideally, the inclusion of trans-oceanic DART stations can aid in the modeling of offshore slip through additional observations over a wider azimuth range. However, this also requires the inclusion of the accumulating effects of dispersion and possibly the elastic loading of the seafloor from the propagating wave. These effects not only change the arrival

time of the wave at far-field stations, when compared to linear long wave models, but they also distort the waveform itself [Watada *et al.*, 2014]. While it is possible to address some of these distortions [e.g. Watada *et al.*, 2014], we exclude use of the far-field tsunami waveforms because they are expected to have much less sensitivity to the details of the slip distribution than the near-field waveforms used here [Geist and Dmowska, 1999].

Most earthquakes exhibit rupture speeds up to 3km/s in subduction zone environments [e.g. Bilek and Lay, 1999]. However, in the case of slow, tsunami earthquakes, rupture can be substantially reduced, down to as little as 1 km/s, greatly extending the duration of rupture [Kanamori, 1972], and substantially diminishing the propagated energy, as was the case in the 1996 Chimbote, Peru earthquake (Figure 1) [Newman and Okal, 1998]. The slowed rupture is sometimes attributed to slip in the shallowest portion of the interface near the trench [e.g. Bilek and Lay, 1999; Polet and Kanamori, 2000]. Based on teleseismic energy back-projections, Yin *et al.* [2016] identified a substantial and slow delayed rupture component to the 2015 Illapel earthquake, extending between 80 and 130 s from the initial rupture, with the patch occurring up-dip of the initial nucleation, and very near the trench. Using a teleseismic inversion of the spectral contributions from the Illapel earthquake, Lee *et al.* [2016] similarly found a two-stage rupture process, but with moderately longer durations, the first lasting 100 s, and the second not terminating until about 250 s after the rupture initiation.

Examination of the real-time radiated energy growth, automatically ran at Georgia Tech using RTerg [Convers and Newman, 2011], shows that this earthquake does indeed exhibit complex, and delayed energy release that is discernable within the cumulative growth of high-frequency (0.5-2 Hz) teleseismically radiated P-wave energy (Figure 7). While the automated algorithm estimated the rupture duration,  $T_R$ , at 135 s using the cross-over between the rapid initial growth and the later slow-growth of high-frequency energy, the steeply-

sloped growth phase uncharacteristically exhibits a break in the linear slope. Unlike most other earthquakes which exhibit a simple singular growth phase, this event has a more-rapid growth period that terminates at 83 s, followed by a more slowly growing phase that terminates near 146 s. *Newman et al.* [2011], using the 2010 Mentawai tsunami earthquake, identified that such a depressed growth is characteristic of slow rupture. Interestingly, these windows correspond well with the two periods found by *Yin et al.* [2016], that also identified the second stage as growing more slowly. Furthermore, the real-time energy result culminated in a high-frequency energy magnitude,  $M_{e-hf} = 7.8$  (corresponding to  $3.0 \times 10^{15}$  J), 0.5 units smaller than  $M_W$  (8.3) as reported by gCMT. Such a feature is comparable to the deficiency in the Theta parameter ( $\Theta = \text{Log}_{10}(E/M_0)$ ), originally described as characteristic for slow tsunami earthquakes in *Newman and Okal* [1998]. Thus, while our joint inversion that includes DART data suggests the most up-dip component of the megathrust is not responsible for the tsunami generated, a number of results strongly support the likelihood of a slowed, and possibly near-trench component: 1) the back-projections of *Yin et al.* [2016]; 2) the spectral analysis of *Lee et al.* [2016]; and 3) the slowed secondary growth and reduced overall earthquake energy following *Convers and Newman* [2011]. While it is likely that the second and slowed phase of energy release contributed to the overall tsunami, it is not clear that significant fractions of the slip for this component occurred near the trench. If the slowed phase did occur near the trench, it is possible that the dip angle is so low that it had an inappreciable contribution to tsunami generation.

## 6. Conclusion

We conduct a trans-coastal joint inversion to solve for coseismic slip along the subduction megathrust using deep-ocean pressure gauge tsunami time series, continuous GPS, and Sentinel-1A InSAR data following the 2015 Illapel earthquake. By supplementing

the traditional land-based geodetic slip inversion with a tsunami dataset, key information about the region between the trench and the coast can be incorporated, substantially increasing the resolution domain for megathrust events. Our preferred result has a large concentration of slip near the coastline and down-dip from the trench axis, but still under a submarine environment, leading to tsunami excitation. Our model is in good agreement with tsunami time series recorded at four nearby DART gauges, with little phase delay between the modeled tsunami arrival and the observed time series, and a consistent peak amplitude for the initial part of the tsunami, before the inclusions of coastal reflections. Unlike other models, this result does not require the earthquake to rupture the near-trench region of the megathrust in order to fit the timing or magnitude of the observed tsunami. The incorporation of tsunami data into the inversion processes provides a useful dataset for constraining offshore slip in a region that is otherwise difficult to resolve through geodetic means. Consistent use of tsunami data, when available, for future earthquakes will allow for a clearer understanding of when there is and is not shallow slip on the megathrust. When applied, this data allows for a better assessment of the diverse tsunamigenic behavior of earthquakes along the Peru–Chile trench, but can also be included in studies of other seismically active regions.

## **7. Acknowledgements**

This research was supported through State Funds through Georgia Tech to AVN as well as through the National Science Foundation East Asian and Pacific Summer Institute project 1614142. P. Cummins was partially supported by Australian Research DP120103297. Figures were generated using Generic Mapping Tools from *Wessel et al.* [2013]. We appreciate the openly available and processed Sentinel-1 InSAR data and open ocean tsunami waveform datasets that were made accessible by the European Space Agency and the US National Oceanic and Atmospheric Administration, respectively. GPS data was recorded by the National Seismological Center of the Universidad de Chile and processed by J Baez. Finally, we thank Emma Hill and two anonymous reviewers for their constructive comments.

## 8. References

- An, C., I. Sepúlveda, PLF. Liu (2014), Tsunami source and its validation of the 2014 Iquique, Chile Earthquake, *Geophys. Res. Lett.*, 41, 3988–3994, doi:[10.1002/2014GL060567](https://doi.org/10.1002/2014GL060567).
- Baba, T., N. Takahashi, Y. Kaneda, K. Ando, D. Matsuoka, T. Kato (2015), Parallel implementation of dispersive tsunami wave modeling with a nesting algorithm for the 2011 Tohoku Tsunami. *Pure and Applied Geophysics* 172.12: 3455-3472.
- Benavente, R, PR. Cummins, J Dettmer (2016), Rapid automated W-phase slip inversion for the Illapel great earthquake (2015, Mw= 8.3). *Geophys. Res. Lett.*, 43.5: 1910-1917.
- Bilek, S.L. and T. Lay (1999), Rigidity variations with depth along interplate megathrust faults in subduction zones. *Nature*, 400(6743), pp.443-446.
- Bourgeois, J., C. Petroff, H. Yeh, V. Titov, C.E. Synolakis, B. Benson, J. Kuroiwa, J. Lander, E. Norabuena (1999), Geologic Setting, Field Survey and Modeling of the Chimbote, Northern Peru, Tsunami of 21 February 1996. In *Seismogenic and Tsunamigenic Processes in Shallow Subduction Zones* (pp. 513-540). Birkhäuser Basel. doi:[10.1007/s000240050242](https://doi.org/10.1007/s000240050242)
- Calisto, I., M. Miller, and I. Constanzo (2016), Comparison between tsunami signals generated by different source models and the observed data of the Illapel 2015 earthquake. *Pure and Applied Geophysics*, 173.4: 1051-1061.
- Chen, T., A. V. Newman, L. Feng, H. M. Fritz (2009), Slip Distribution from the 1 April 2007 Solomon Islands Earthquake: A Unique Image of Near-Trench Rupture, *Geophys. Res. Lett.*, 36, L16307, doi:[10.1029/2009GL039496](https://doi.org/10.1029/2009GL039496).
- Convers, J. A., A. V. Newman (2011), Global Evaluation of Large Earthquake Energy from 1997 Through mid-2010, *J. Geophys. Res.*, 116, B08304, doi:[10.1029/2010JB007928](https://doi.org/10.1029/2010JB007928).
- DeMets, C., R.G. Gordon, D.F. Argus (2010), Geologically current plate motions. *Geophysical Journal International*, 181(1), pp.1-80. doi: [10.1111/j.1365-246X.2009.04491.x](https://doi.org/10.1111/j.1365-246X.2009.04491.x)
- Ekström, G., M. Nettles, A.M. Dziewoński (2012), The global CMT project 2004–2010: centroid-moment tensors for 13,017 earthquakes. *Physics of the Earth and Planetary Interiors*, 200, pp.1-9. doi:[10.1016/j.pepi.2012.04.002](https://doi.org/10.1016/j.pepi.2012.04.002)
- Fritz, H.M., C.M. Petroff, P.A. Catalán, R. Cienfuegos, P. Winckler, N. Kalligeris, R. Weiss, S.E. Barrientos, G. Meneses, C. Valderas-Bermejo, C. Ebeling (2011). Field survey of the 27 February 2010 Chile tsunami. *Pure and Applied Geophysics*, 168(11), pp.1989-2010. doi: [10.1007/s00024-011-0283-5](https://doi.org/10.1007/s00024-011-0283-5)
- Geist, E.L., and R. Dmowska (1999), Local tsunamis and distributed slip at the source: *Pure and Applied Geophysics*, v. 154, p. 485-512.

Gica, E., M.C. Spillane, V. Titov, C.D. Chamberlin, J.C. Newman (2008). Development of the Forecast Propagation Database for NOAA's Short-Term Inundation Forecast for Tsunamis(SIFT).

Grandin, R., E. Klein, M. Métois, C. Vigny (2016), Three-dimensional displacement field of the 2015 Mw8.3 Illapel earthquake (Chile) from across- and along-track Sentinel-1 TOPS interferometry, *Geophys. Res. Lett.*, 43, 2552–2561, doi:[10.1002/2016GL067954](https://doi.org/10.1002/2016GL067954).

Gusman, A. R., Y. Tanioka, T. Kobayashi, H. Latief, and W. Pandoe (2010), Slip distribution of the 2007 Bengkulu earthquake inferred from tsunami waveforms and InSAR data, *J. Geophys. Res.*, 115, B12316, doi:[10.1029/2010JB007565](https://doi.org/10.1029/2010JB007565).

Gusman, A. R., S. Murotani, K. Satake, M. Heidarzadeh, E. Gunawan, S. Watada, B. Schurr, (2015), Fault slip distribution of the 2014 Iquique, Chile, earthquake estimated from ocean-wide tsunami waveforms and GPS data. *Geophys. Res. Lett.*, 42: 1053–1060. doi:[10.1002/2014GL062604](https://doi.org/10.1002/2014GL062604).

Harris, R. A., P. Segall (1987), Detection of a locked zone at depth on the Parkfield, California, segment of the San Andreas Fault, *J. Geophys. Res.*, 92(B8), 7945–7962, doi:[10.1029/JB092iB08p07945](https://doi.org/10.1029/JB092iB08p07945).

Hayes, G. P., M.W. Herman, W.D. Barnhart, K.P. Furlong, S. Riquelme, H.M. Benz, E. Bergman, S. Barrientos, P. S. Earle, S. Samsonov (2014), Continuing megathrust earthquake potential in Chile after the 2014 Iquique earthquake, *Nature*, 512(7514), 295–298, doi:[10.1038/nature13677](https://doi.org/10.1038/nature13677).

Hayes, G. P., D. J. Wald, R. L. Johnson (2012), Slab1.0: A three-dimensional model of global subduction zone geometries, *J. Geophys. Res.*, 117, B01302, doi:[10.1029/2011JB008524](https://doi.org/10.1029/2011JB008524).

Heidarzadeh, M., S. Murotani, K. Satake, T. Ishibe, A. R. Gusman (2016), Source model of the 16 September 2015 Illapel, Chile,  $M_w$  8.4 earthquake based on teleseismic and tsunami data, *Geophys. Res. Lett.*, 43, 643–650, doi:[10.1002/2015GL067297](https://doi.org/10.1002/2015GL067297).

Heinrich, P., F. Schindele, S. Guibourg, P.F. Ihmlé, 1998. Modeling of the February 1996 Peruvian tsunami. *Geophysical research letters*, 25(14), pp.2687-2690.

Hsu, Y.J., M. Simons, J.P. Avouac, J. Galetzka, K. Sieh, M. Chlieh, D. Natawidjaja, L. Prawirodirdjo, Y. Bock (2006). Frictional afterslip following the 2005 Nias-Simeulue earthquake, Sumatra. *Science*, 312(5782), pp.1921-1926. DOI: [10.1126/science.1126960](https://doi.org/10.1126/science.1126960)

Jónsson, S., H. Zebker, P. Segall, F. Amelung (2002). Fault slip distribution of the 1999 Mw 7.1 Hector Mine, California, earthquake, estimated from satellite radar and GPS measurements. *Bulletin of the Seismological Society of America*, 92(4), pp.1377-1389.

Kajiura, K. (1963) The Leading Wave of a Tsunami, *Bulletin of the Seismological Society of America*.

Kanamori, Hiroo, (1972), Mechanism of tsunami earthquakes, *Physics of the earth and planetary interiors* 6.5: 346-359. doi:10.1016/0031-9201(72)90058-1

Lee, S.J., T.Y. Yeh, T.C. Lin, Y.Y. Lin, T.R. Song, B.S. Huang (2016), Two-stage composite megathrust rupture of the 2015  $M_w$ 8.4 Illapel, Chile, earthquake identified by spectral-element inversion of teleseismic waves, *Geophys. Res. Lett.*, 43, doi:10.1002/2016GL068843.

Li, L., T. Lay, K. F. Cheung, and L. Ye (2016), Joint modeling of teleseismic and tsunami wave observations to constrain the 16 September 2015 Illapel, Chile,  $M_w$  8.3 earthquake rupture process, *Geophys. Res. Lett.*, 43, 4303–4312, doi:10.1002/2016GL068674.

Lorito, S., F. Romano, S. Atzori, X. Tong, A. Avallone, J. McCloskey, M. Cocco, E. Boschi, A. Piatanesi (2011), Limited overlap between the seismic gap and coseismic slip of the great 2010 Chile earthquake, *Nature*, 4(3), 173–177, doi:10.1038/ngeo1073.

Malservisi, R., Schwartz, S.Y., Voss, N., Protti, M., Gonzalez, V., Dixon, T.H., Jiang, Y., Newman, A.V., Richardson, J., Walter, J.I. and Voyenko, D., 2015. Multiscale postseismic behavior on a megathrust: The 2012 Nicoya earthquake, Costa Rica. *Geochemistry, Geophysics, Geosystems*, 16(6), pp.1848-1864. doi:10.1002/2015GC005794.

Moreno, M., D. Melnick, M. Rosenau, J. Bolte, J. Klotz, H. Echtler, J. Baez, K. Bataille, J. Chen, M. Bevis, H. Hase (2011). Heterogeneous plate locking in the South–Central Chile subduction zone: Building up the next great earthquake. *Earth and Planetary Science Letters*, 305(3), pp.413-424. doi:10.1016/j.epsl.2011.03.025

Moreno, M., M. Rosenau, O. Oncken (2010), 2010 Maule earthquake slip correlates with pre-seismic locking of Andean subduction zone. *Nature*, 467(7312), pp.198-202. doi:10.1038/nature09349

Newman, A. V. & E. A. Okal (1998), Teleseismic Estimates of Radiated Seismic Energy: The  $E/M_0$  Discriminant for Tsunami Earthquakes, *Jour. of Geoph. Res.*, 103 (11), 26,885-98.

Newman, A. V., G. Hayes, Y. Wei, J. A. Convers (2011), The 25 October 2010 Mentawai Tsunami Earthquake, from real-time discriminants, finite-fault rupture, and tsunami excitation, *Geophys. Res. Lett.*, 38, L05302, doi:10.1029/2010GL046498.

Newman, A. V., L. Feng, H. M. Fritz, Z. M. Lifton, N. Kalligeris, and Y. Wei (2011), The Energetic 2010  $M_w$  7.1 Solomon Islands Tsunami Earthquake *Geophys. Journ. Int.*, 186 (2), 775–781, doi:10.1111/j.1365-246X.2011.05057.x.

Newman, A. V. (2011). Hidden depths. *Nature*, 474(7352), 441-443. doi:10.1038/474441a

National Geophysical Data Center database (NGDC). <https://www.ngdc.noaa.gov>. (accessed: 15.05.16)

Okada, Y., (1985). Surface deformation due to shear and tensile faults in a half-space. *Bulletin of the seismological society of America*, 75(4), pp.1135-1154.

Plafker, G. & Savage, J.C. (1970), Mechanism of the Chilean Earthquakes of May 21 and 22, 1960, *Geol. Soc. Am. Bull.*, 81, 1001–1030.

Polet, J. and Kanamori, H., 2000. Shallow subduction zone earthquakes and their tsunamigenic potential. *Geophysical Journal International*, 142(3), pp.684-702.

Satake, K., (1994). Mechanism of the 1992 Nicaragua tsunami earthquake. *Geophysical Research Letters*, 21(23), pp.2519-2522.

Schurr, B., Asch, G., Hainzl, S., Bedford, J., Hoechner, A., Palo, M., Wang, R., Moreno, M., Bartsch, M., Zhang, Y. and Oncken, O., (2014). Gradual unlocking of plate boundary controlled initiation of the 2014 Iquique earthquake. *Nature*, 512(7514), pp.299-302. doi:10.1038/nature13681

Tang, L., V. Titov, C. Moore, Y. Wei (2016). Real-time assessment of the 16 September 2015 Chile tsunami and implications for near-field forecast. *Pure and Applied Geophysics*, 173(2), pp.369-387. doi:10.1007/s00024-015-1226-3

Tilmann, F., Y. Zhang, M. Moreno, J. Saul, F. Eckelmann, M. Palo, Z. Deng, A. Babeyko, K. Chen, J.C. Baez, B. Schurr, R. Wang, T. Dahm (2016) The 2015 Illapel earthquake, central Chile: A type case for a characteristic earthquake? *Geophysical Research Letters*, 43, 574-583, doi:10.1002/2015GL066963.

Titov, V.V. C.E. Synolakis (1998). Numerical modeling of tidal wave run-up. *Journal of Waterway, Port, Coastal, and Ocean Engineering*, 124(4), pp.157-171.

Titov, V.V. F.I. Gonzalez (1997). Implementation and testing of the method of splitting tsunami (MOST) model. US Department of Commerce, National Oceanic and Atmospheric Administration, Environmental Research Laboratories, Pacific Marine Environmental Laboratory.

Vigny, C., A. Rudloff, J.C. Ruegg, R. Madariaga, J. Campos, J. M. Alvarez (2009), Upper plate deformation measured by GPS in the Coquimbo Gap, Chile. *Physics of the Earth and Planetary Interiors*, 175(1), pp.86-95. doi:10.1016/j.pepi.2008.02.013

Accepted Article  
Watada, S., S. Kusumoto, K. Satake (2014), Traveltime delay and initial phase reversal of distant tsunamis coupled with the self-gravitating elastic Earth, *Journal of Geophysical Research: Solid Earth* 119.5: 4287-4310.

Wessel, P., W. H. F. Smith, R. Scharroo, J. F. Luis, and F. Wobbe (2013), Generic Mapping Tools: Improved version released, *EOS Trans. AGU*, 94, 409-410.

Ye, L., T. Lay, H. Kanamori, KD Koper (2016), Rapidly estimated seismic source parameters for the 16 September 2015 Illapel, Chile  $M_w$  8.3 earthquake. *Pure and Applied Geophysics* 173.2: 321-332.

Yin, J., H. Yang, H. Yao, H. Weng (2016), Coseismic radiation and stress drop during the 2015 $M_w$  8.3 Illapel, Chile megathrust earthquake, *Geophys. Res. Lett.*, 43, 1520–1528, doi:[10.1002/2015GL067381](https://doi.org/10.1002/2015GL067381).

Yue, H., T. Lay, L. Rivera, C. An, C. Vigny, X. Tong, J. C. Báez Soto (2014), Localized fault slip to the trench in the 2010 Maule, Chile  $M_w = 8.8$  earthquake from joint inversion of high-rate GPS, teleseismic body waves, InSAR, campaign GPS, and tsunami observations, *J. Geophys. Res. Solid Earth*, 119, 7786–7804, doi:[10.1002/2014JB011340](https://doi.org/10.1002/2014JB011340).

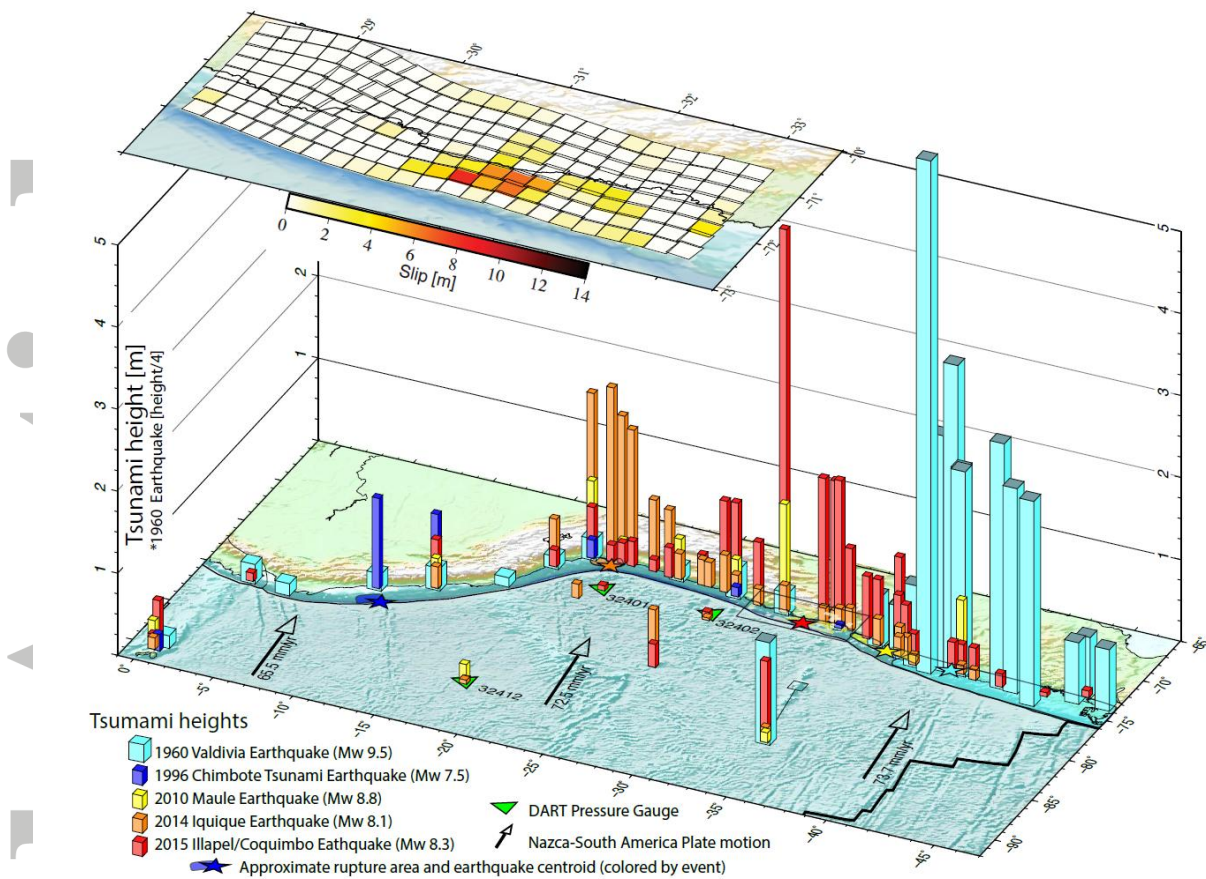


**Figure 1.** Regional map of past tsunamigenic earthquakes and their generated tsunamis. The epicenter of the 1960 and centroid location for later events [Ekström *et al.*, 2012] with the approximate rupture area are shown by colored stars and transparent polygons beneath [Bourgeois *et al.*, 1999; Lorito *et al.*, 2011; Hayes *et al.*, 2014]. For each event, the regional tsunami wave height measured by local tide gauges and deep-water pressure sensors (green triangles) are shown as columnar bars (1960 is augmented by eyewitness accounts (gray tops, and are all divided by 4 to stay on scale) [NGDC, 2016]. The Nazca plate motion relative to a stable South American plate is also shown (black arrows) [DeMets *et al.*, 2010]. Inset figure: preferred fault plane solution using GPS, InSAR, and tsunami datasets.

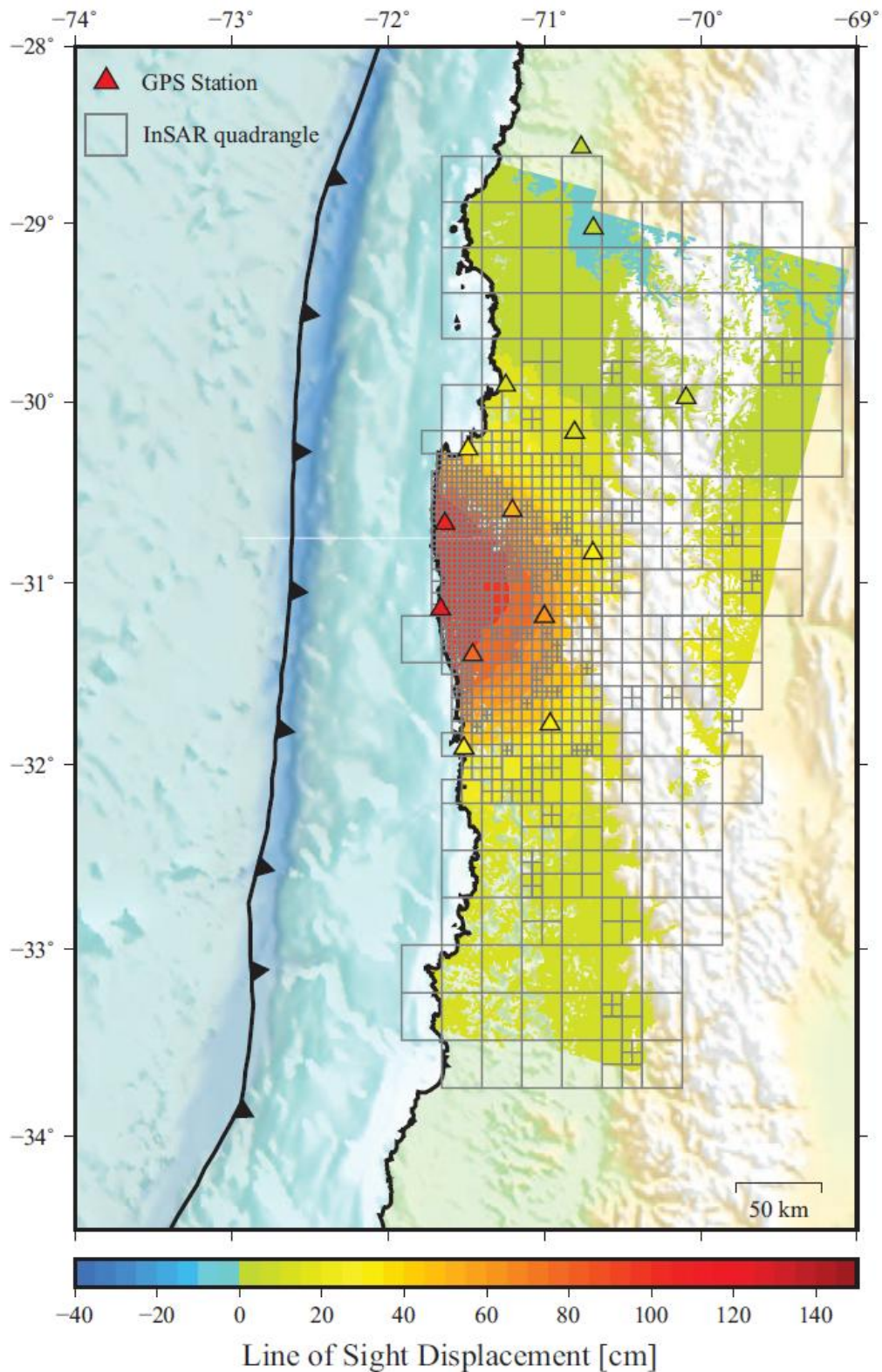


**Figure 2.** Regional InSAR derived displacements in the direction of satellite line-of-sight with Quadtree discretization (grey boxes). Each box represents one point used in the inversion. Triangles indicate the location of the nearby GPS stations. The color of each triangle is the magnitude of displacement of the three component GPS when translated into the line-of-sight direction. The matching colors between the InSAR displacement field and the GPS shows that both datasets are consistent with each other.

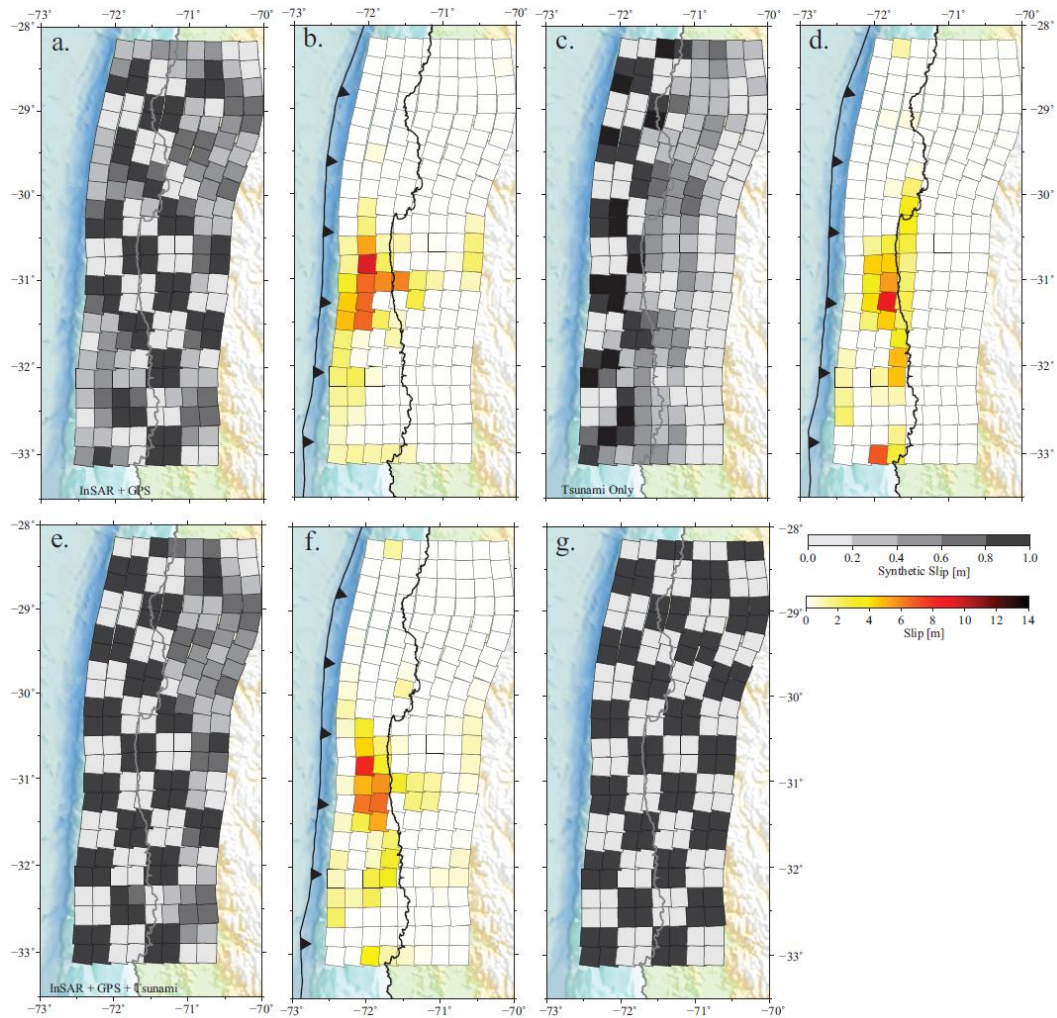


**Figure 3.** “Checkerboard” resolution tests. (a) geodetic only checkerboard solution, using only the InSAR and GPS datasets; (b) preferred model results from an InSAR and GPS dataset; (c) checkerboard solution incorporating only DART tsunami waveforms; (d) preferred model results from a tsunami dataset; (e) checkerboard solution using all available data. (f) preferred slip solution using all data; (g) initial checkerboard input with 50 x 50 km checkers alternating between 0 and 1 meter of dip slip; Solutions in b & c illustrate the spatial variability and limitations of using geodetic and tsunami datasets, respectively.

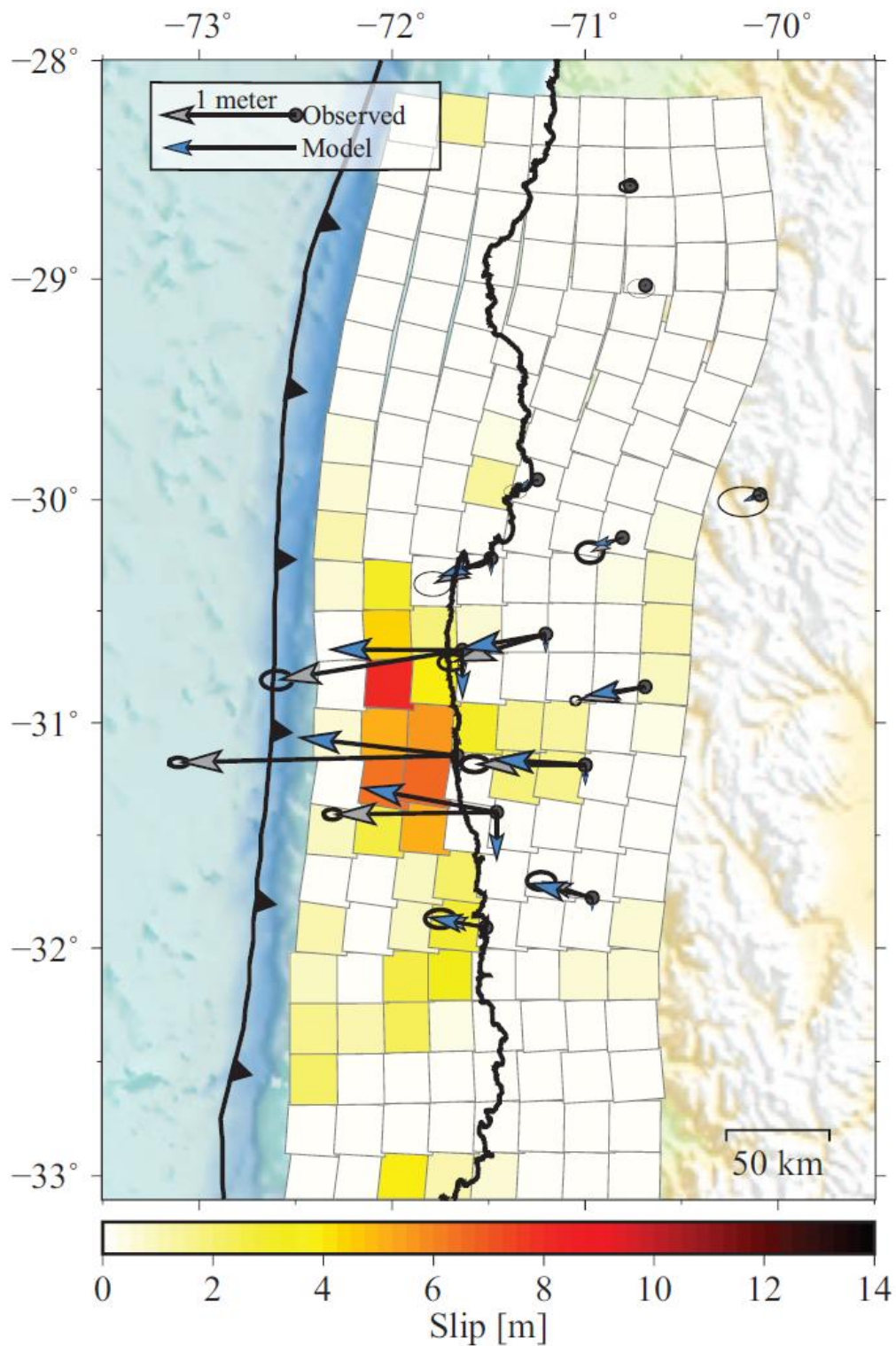


**Figure 4.** Observed (gray) and modeled (blue) horizontal and vertical coseismic GPS coseismic displacements superimposed on the preferred slip model (repeated from Figure 3f).

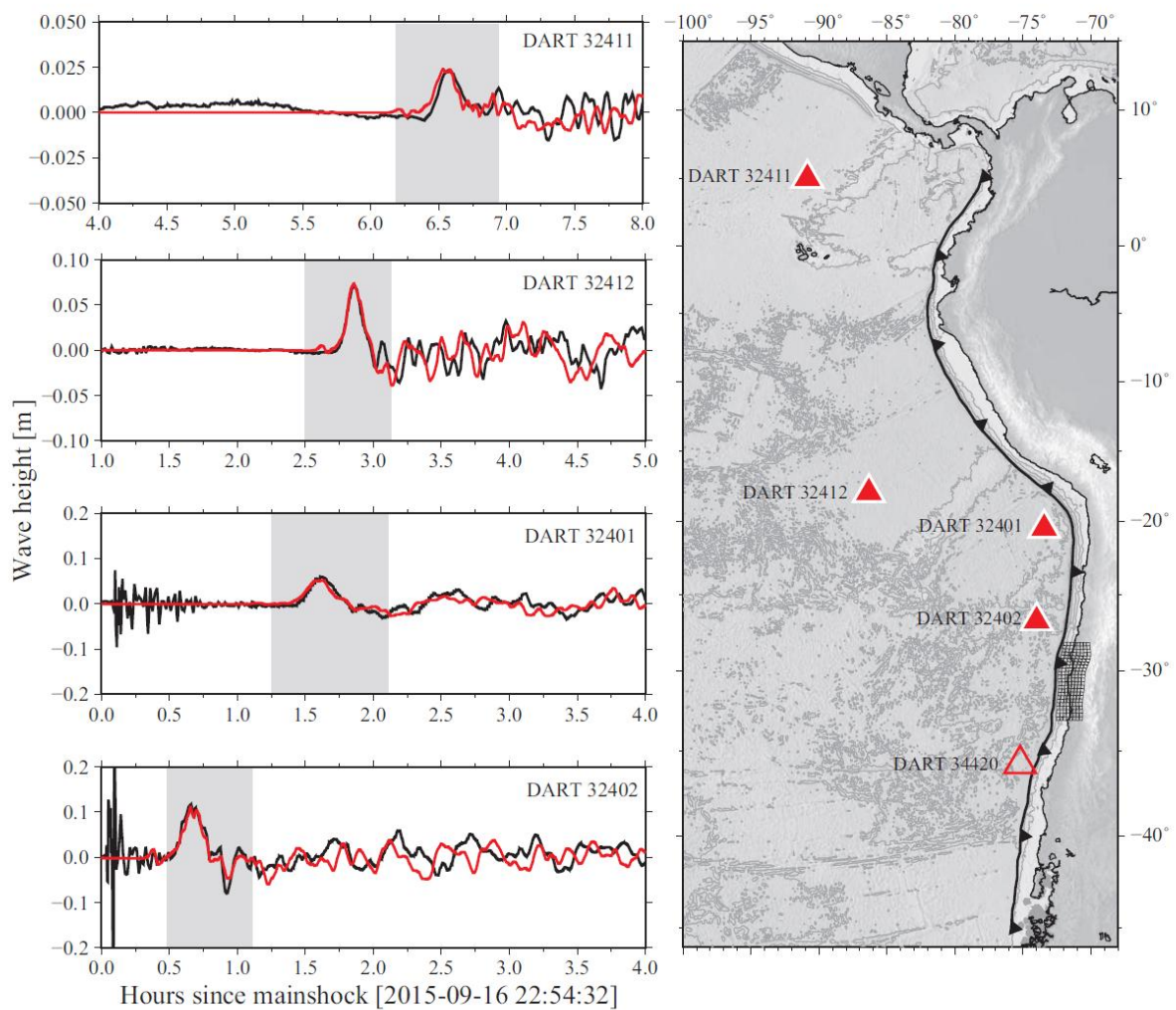


**Figure 5.** (a) Black line: recorded tsunami waveforms from the four nearest and active DART pressure gauges with timing relative to the mainshock. Red line: forward simulated tsunami result for preferred model. The gray boxes in each of the four subplots highlights the windowed region used in the inversion process. Regions were picked to include the first and largest amplitude part of the tsunami while excluding surface wave recordings and later coastal reflections. Both of the excluded effects cannot be modeled through our inversion process. (b) Geographic distribution of nearby DART gauges active during the earthquake (red solid triangles). The discretized fault plane is shown near 30°S. The hollow triangle outlined in red is the newest addition to the DART gauge fleet along the Peru-Chile trench, but was not active during the tsunami.

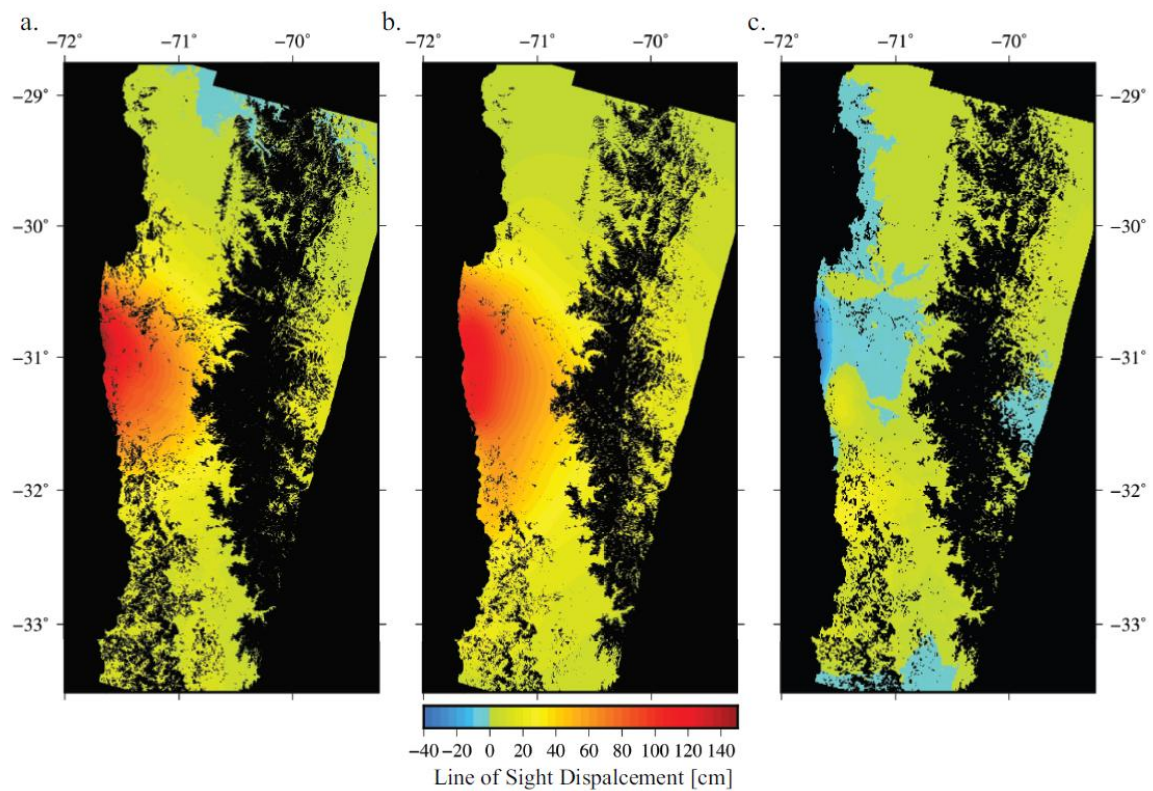


**Figure 6.** Comparison of InSAR line-of-sight (LOS) change for data and our preferred model. (a) Observed LOS displacement, repeated from Figure 2. (b) LOS projection of the preferred model results. (c) Residual LOS displacement, determined by removing the predicted (b) from the observed (a) signal.

Accepted

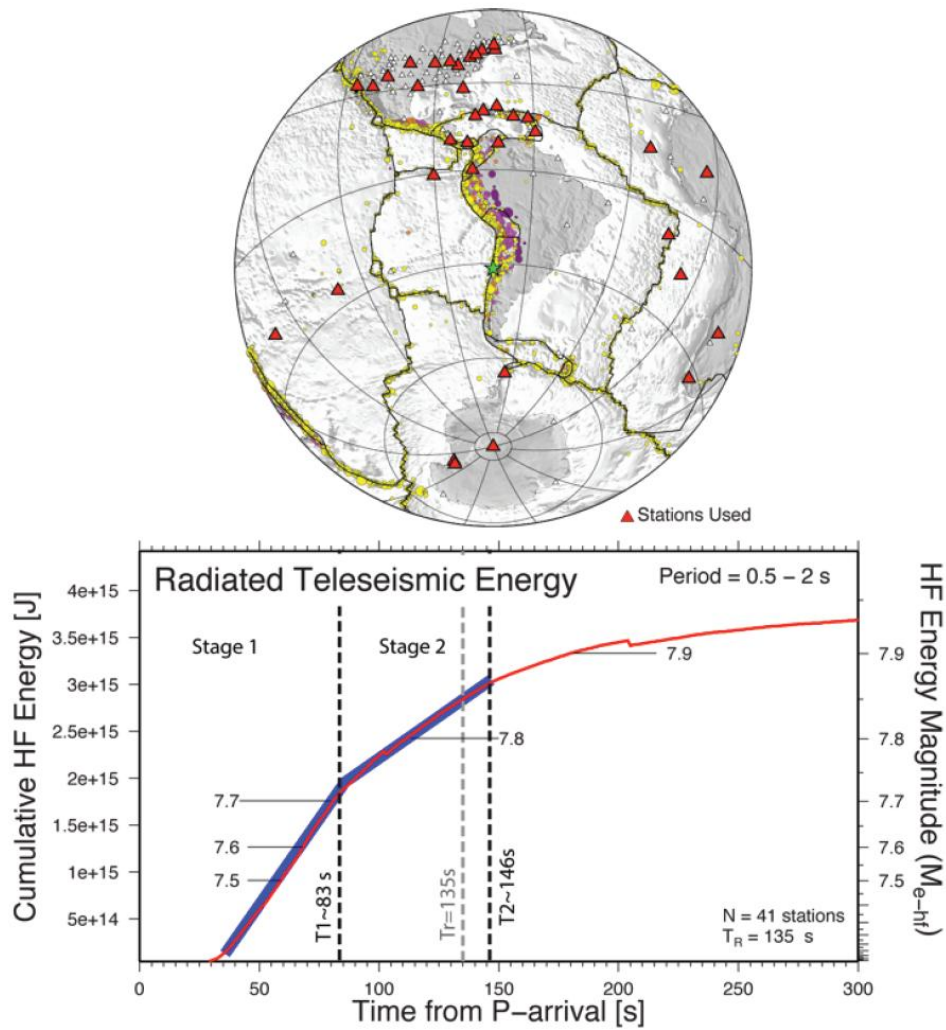


**Figure 7.** The cumulative high-frequency energy radiated from the Illapel earthquake is shown (red line) using data from 41 seismic stations available in real-time (red triangles in map) and automatically processed following *Convers and Newman* [2011]. The automated rupture duration,  $T_R$  (dashed gray line), two near-linear periods of growth (denoted by thick blue lines) and their termination times relative to the earthquake nucleation (dashed black lines). The cumulative energy is converted to a high-frequency energy magnitude, which appears deficient for this event, similar but more moderate than slow-rupturing tsunami earthquakes.